Identification of quartzofeldspathic materials on Mars

Joshua L. Bandfield,[1] Victoria E. Hamilton,[2] Philip R. Christensen,[1]
and Harry Y. McSween Jr.[3]

Received 4 May 2004; revised 14 July 2004; accepted 18 August 2004; published 21 October 2004.

[1] A unique spectral component has been identified near and on the central peaks of two 30 km diameter craters in northern Syrtis Major. These exposures are clearly visible in Thermal Emission Imaging System (THEMIS) color radiance images as well as THEMIS and Thermal Emission Spectrometer (TES) surface emissivity data. Both TES and THEMIS data indicate the presence of increased 1050–1250 cm^{-1} (~8–9.5 μm) absorption compared to the surrounding basaltic plains, and TES data also display other absorptions at 400, 470, and 800 cm^{-1} (~25, 20, and 12 μm) consistent with the presence of quartz. Ratio and isolated central peak spectral unit spectra match laboratory emissivity spectra of granitoid rocks composed primarily of quartz and plagioclase feldspar. Deconvolution results also indicate that the surface contains quartz and feldspar in addition to a high-Si glass and/or sheet silicate component. Because central peak materials are brought up from depth during the cratering event, the association of the quartzofeldspathic mineralogy with the central peaks of the craters indicates that the quartz-bearing material was excavated from depth. The occurrence in the two adjacent craters may imply a granitoid pluton of considerable extent. A plausible formation mechanism for this relatively silicic material may be similar to that of terrestrial trondhjemites, which do not require plate tectonics. The rarity of the exposures implies that the process that formed the granitoid composition was probably not widespread. The presence of quartz-bearing material on Mars indicates that mechanisms that produce highly differentiated magmas have been present and extends the diversity of surface compositions identified. *INDEX TERMS:* 6225 Planetology: Solar System Objects: Mars 5464 Planetology: Solid Surface Planets: Remote sensing; 5470 Planetology: Solid Surface Planets: Surface materials and properties; 5494 Planetology: Solid Surface Planets: Instruments and techniques; 5410 Planetology: Solid Surface Planets: Composition; *KEYWORDS:* infrared spectroscopy, Mars mineralogy

Citation: Bandfield, J. L., V. E. Hamilton, P. R. Christensen, and H. Y. McSween Jr. (2004), Identification of quartzofeldspathic materials on Mars, *J. Geophys. Res.*, *109*, E10009, doi:10.1029/2004JE002290.

1. Introduction

[2] Martian meteorites and remote sensing have revealed a variety of Martian surface and crustal compositions. Telescopic and spacecraft near-infrared observations have revealed variable ~1 and 2 μm absorptions indicative of an assortment of pyroxene compositions [*Adams*, 1968; *Singer et al.*, 1979; *Singer and McSween*, 1993; *Mustard et al.*, 1993, 1997] and abundant evidence of Fe^{3+} mineralogies in both high- and low-albedo regions [e.g., *Soderblom et al.*, 1978; *McCord et al.*, 1982; *Murchie et al.*, 1993; *Geissler et al.*, 1993; *Merenyi et al.*, 1996; *Bell and Morris*, 1999; *Bell et al.*, 2000; *Morris et al.*, 2000]. Measurements from Thermal Emission Spectrometer (TES) onboard the Mars Global Surveyor spacecraft have been used to identify several global surface compositions. Low-albedo regions are dominated by two distinct compositions; a basaltic composition dominated by plagioclase and high-Ca pyroxene and a composition consisting primarily of plagioclase and high-Si glass [*Bandfield et al.*, 2000a; *Hamilton et al.*, 2001; *Bandfield*, 2002]. This second composition can be interpreted as andesitic if the glass component is primary [*Bandfield et al.*, 2000a; *Hamilton et al.*, 2001], but the glass could also be secondary [*Minitti et al.*, 2002; *Wyatt and McSween*, 2002; *Kraft et al.*, 2004].

[3] Local-to-regional exposures of other compositions have been identified using TES data. High concentrations of olivine have been located in isolated locations, such as Nili Fossae [*Hoefen et al.*, 2003; *Hamilton et al.*, 2003], and surface mineralogy similar to the orthopyroxenite ALH84001 (Allen Hills meteorite sample number 1 collected in 1984) has been identified in Eos Chasma [*Hamilton et al.*, 2003]. Exposures of grey crystalline hematite are located in Sinus Meridiani, Aram Chaos, and Ophir and Candor Chasmas [*Christensen et al.*, 2000, 2001a].

[1]Department of Geological Sciences, Arizona State University, Tempe, Arizona, USA.
[2]Hawai'i Institute of Geophysics and Planetology, University of Hawai'i, Honolulu, Hawai'i, USA.
[3]Department of Earth and Planetary Sciences, University of Tennessee, Knoxville, Tennessee, USA.

0148-0227/04/2004JE002290$09.00

[4] TES data have been used to constrain the mineralogy of the Martian dust. *Bandfield and Smith* [2003] isolated the spectral shape of high-albedo surfaces that display evidence for framework silicates such as plagioclase or zeolites and bound water [*Bandfield and Smith*, 2003; *Ruff*, 2004] as well as low concentrations of carbonates [*Bandfield et al.*, 2003].

[5] Martian meteorites are composed of a range of mafic lithologies, including dominantly olivine or pyroxene cumulates and a variety of basaltic compositions [e.g., *McSween*, 1994]. Viking and Mars Pathfinder chemistry measurements of the Martian fines are also consistent with mafic compositions as well as abundant sulfur-bearing compositions [*Toulmin et al.*, 1977; *McSween and Keil*, 2000; *Bell et al.*, 2000]. Alpha proton X-ray spectrometer results also suggest andesitic compositions at the Mars Pathfinder landing site [*McSween et al.*, 1999; *Foley et al.*, 2003].

[6] The combined set of observations, though not without controversy and debate, generally points to low-albedo surface compositions dominated by mafic and possibly intermediate igneous materials with limited chemical alteration. High abundances of widespread secondary minerals, such as clays or carbonates, are not present (though sulfates are expected globally [e.g., *Clark et al.*, 1982] and have been identified locally [*Morris et al.*, 2004]). Metamorphic compositions have not been identified using either remote sensing observations or the Martian meteorites.

[7] This work describes the identification of a local quartz-bearing material that is likely igneous in origin. Though the process that formed this composition does not necessarily occur planetwide, it does indicate that mechanisms that produce highly differentiated magmas have operated on Mars. The results presented here extend the diversity of Martian surface compositions identified. This variety of surface and crustal compositions indicates that Mars has had a complex igneous history.

2. Approach

2.1. Data Sets

[8] A variety of data sets were used for this study, including the Thermal Emission Imaging System (THEMIS) visible and near-infrared multispectral images, THEMIS multispectral thermal infrared images, TES spectroscopic data, Mars Orbiter Camera (MOC), and Mars Orbiter Laser Altimeter (MOLA) elevation data. The combination of the data sets, especially TES and THEMIS thermal infrared (TIR) data, allows for a more complete characterization of the area of interest as well as independent verification of the results of each data set.

2.1.1. THEMIS Infrared

[9] The THEMIS instrument consists of TIR and visible/near-infrared imagers. The TIR portion of THEMIS consists of an uncooled 320 by 240 element microbolometer array with nine spectral channels centered from 6.5 to 15 μm (Table 1), and images are assembled in a push broom fashion. Spatial sampling is 100 m from the 420 km altitude circular orbit of Mars Odyssey. An internal calibration flag and instrument response functions determined from prelaunch data are used to produce calibrated radiance images. *Christensen et al.* [2004] and *Bandfield et al.* [2004] present more thorough descriptions of random and systematic uncertainties. The THEMIS infrared (IR) data were used to determine and map spectral units and perform coarse compositional analysis. Nighttime THEMIS IR data were used to determine thermophysical characteristics of the surface.

Table 1. THEMIS Band Centers and Widths

Band	Center Wavelength, μm	Band Width, μm[a]
1	6.27	1.01
2	6.27	1.01
3	7.38	1.09
4	7.98	1.16
5	8.75	1.20
6	9.66	1.10
7	10.45	1.19
8	11.26	1.07
9	12.17	0.81
10	14.45	0.87

[a]Band width is measured at full width at half maximum.

2.1.2. TES

[10] The TES instrument is a Fourier transform Michelson interferometer that covers the wavelength range from 1700 to 200 cm^{-1} (~6 to 50 μm) at 10 or 5 cm^{-1} sampling [*Christensen et al.*, 1992]. Three cross-track and two along-track detectors provide a spatial sampling of 3 × ~8 km from the final 2 hour, ~380 km altitude mapping orbit. A linear response function for each of the six detectors is derived periodically from observations of space and an internal reference surface of known emissivity and temperature. For a complete description of the TES instrument, operations, and radiometric calibration, see *Christensen et al.* [2001b]. TES data were used to determine the surface mineralogy of the spectral units denoted by the THEMIS data.

2.1.3. THEMIS Visible and Near-Infrared Multispectral Camera (VIS)/MOLA/MOC

[11] Local morphologic characteristics were obtained using the gridded MOLA [*Smith et al.*, 2001] 256 pixel per degree map and visible THEMIS and MOC [*Malin and Edgett*, 2001] images. The laser altimeter data were used to retrieve quantitative morphological characteristics. Both the THEMIS and MOC images were used to determine the relative brightness of surfaces, surface textures, and morphologies. The multispectral THEMIS visible and near-infrared data were also used to determine relative color differences between surfaces. The visible and near-infrared THEMIS imager is a frame imager with five spectral bands centered between 425 and 860 nm assembled in a push broom fashion. Spatial sampling is 18 m $pixel^{-1}$, and pixels can be coadded to increase spectral and spatial coverage.

2.2. THEMIS Analysis Techniques

[12] A number of the THEMIS image analysis techniques described in detail by *Bandfield et al.* [2004] were used to locate and characterize the regions of interest for the work described here. A rapid assessment of spectral variety in a THEMIS image can be completed using decorrelation stretched (DCS) radiance images [*Gillespie et al.*, 1986], which enhance spectral variations present in the three spectral channels used to produce the image. Color DCS TIR radiance images using a variety of spectral band combinations can be produced for THEMIS images with a minimum of processing. This method allows for a coarse

preliminary spectral analysis and reconnaissance of the spectral variety in the THEMIS data set.

[13] Three band combinations are used in this study to examine the bulk of warm (average temperature >240 K) images collected to date: (1) bands 8, 7, and 5; (2) bands 9, 6, and 4; and (3) bands 6, 4, and 2 (Table 1). These three band combination images as well as a gray scale band 9 radiance image are concatenated into a single file. The three different band combination images allow for broad spectral coverage that can be examined quickly.

[14] It is necessary to account for atmospheric emission effects in order to quantitatively compare surface emissivity within any THEMIS image. These effects are removed by the constant radiance offset removal algorithm described by *Bandfield et al.* [2004]. This algorithm uses a designated area of assumed constant emissivity but variable temperature within an image to solve for radiance emitted by the atmosphere as well as radiance from multiple scattering. This accomplishes two tasks: (1) Relative emissivities between surfaces in an image are accurate without any surface temperature dependence. (2) The atmospheric correction problem is greatly simplified and only requires a single multiplicative term for each spectral channel to be determined.

[15] To determine this multiplicative term, low spatial resolution surface emissivity corresponding to a region within the THEMIS image is determined from TES data. This allows the atmospheric opacity contribution in each THEMIS spectral channel to be determined. The opacity values can be applied to individual THEMIS pixels resulting in high spatial resolution surface emissivity [*Bandfield et al.*, 2004]. The relative emissivity errors are $\sim 0-0.003$ for bands 3–9 and ~ 0.01 in bands 1 and 2 for low dust opacity and warm surface temperature conditions present in the data used here [*Bandfield et al.*, 2004].

[16] A linear least squares fit of selected end-members to individual THEMIS pixels provides quantitative compositional information [*Bandfield et al.*, 2004]. This technique also can be used to compensate for spatially variable water ice clouds within a THEMIS scene. End-members can be chosen from the THEMIS scene itself or be convolved to THEMIS spectral resolution from TES or laboratory data. Spectral unit concentration maps have commonly been produced from visible through TIR remote sensing data sets [e.g., *Adams et al.*, 1986; *Mustard and Pieters*, 1987; *Gillespie*, 1992; *Ramsey et al.*, 1999; *Ramsey*, 2002].

2.3. TES Analysis Techniques

[17] All TES data covering the regions of interest located in the THEMIS data were examined using a variety of spectral analysis techniques. Equivalent emissivity spectra (these spectra have atmospheric absorption and emission effects and are not properly called emissivity without qualification) were examined visually for spectral differences. These differences are subtle but systematic and can be identified despite the domination of atmospheric spectral features. Spectral ratios are also useful for accentuating subtle spectral differences between surfaces [*Ruff and Christensen*, 2002].

[18] Atmospherically corrected surface emissivity spectra are necessary for direct comparison to laboratory mineral and rock emissivity measurements. A number of techniques have been developed for use with TES data [*Smith et al.*, 2000; *Bandfield et al.*, 2000b; *Bandfield and Smith*, 2003]. The deconvolution surface atmosphere separation as described by *Smith et al.* [2000], *Bandfield et al.* [2000a, 2000b], and *Bandfield* [2002] was used in the analysis of TES data for this study. This technique allows for the analysis of individual spectra and does not need special multiple emission angle observations or a statistically significant number of spectra for the isolation of each spectral end-member.

[19] The deconvolution surface-atmosphere separation also provides areal mineral and spectral unit abundances that can be used for compositional analysis [*Smith et al.*, 2000; *Bandfield et al.*, 2000a; *Bandfield*, 2002; *Hamilton et al.*, 2003]. Each spectral end-member has an individual uncertainty based on its own spectral contrast and the contrast relative to the combination of other end-members present. A lower limit of 0.10 has been used as the detection limit for most minerals present [*Bandfield*, 2002], though the detection limit can be lower for high spectral contrast minerals such as quartz and olivine [*Hamilton et al.*, 2003]. Previous studies have used averages of a number of TES spectra to derive surface compositional information. The local nature of the unique exposures discussed here requires the use of a limited number of TES pixels, making the uncertainties somewhat higher despite the high temperatures of the TES spectra ($\sim$290 K). Comparison of deconvolution results from individual TES spectra with averages over uniform, warm surfaces indicates the concentration uncertainties are increased to ~ 0.15.

[20] Visual examination of individual spectral features can add confidence in spectroscopic mineral identification, however. Systematic errors may be present that cause the deconvolution algorithm to use specific mineral types to compensate. For example, the deconvolution uses moderate concentrations of carbonates to account for an absorption present at ~ 300 cm^{-1} in the type 1 basaltic terrain [*Bandfield*, 2002]. However, there is no corresponding carbonate absorption present at ~ 1500 cm^{-1} (outside the wavelength range used in the deconvolution algorithm) in the same regions. Conversely, minerals that have relatively prominent, narrow absorptions (e.g., hematite [*Christensen et al.*, 2000]) and are easily identified by eye at concentrations well below the stated detection limit for all minerals present (0.02 rather than 0.10) may be present.

[21] Because the unique lithology that is the subject of this work is observable in TES data, it is possible that other sites with a similar composition could be identified using TES data. One simple means of searching the TES data set for similar lithologies is through the creation of band indices. In this case, the TES spectra known to include the area of interest are used to identify a characteristic spectral feature, such as an emission minimum or maximum, that is (ideally) unique to this lithology. Performing a simple mathematical operation on several channels of TES data that define this characteristic feature creates the index. The index is then calculated for all TES spectra meeting minimum quality criteria, and spectra that are identified as having index values consistent with the presence of the characteristic spectral feature are then examined for spatial correlations that are consistent with either a geologic origin (e.g., spatially extensive, observable in multiple orbits) or

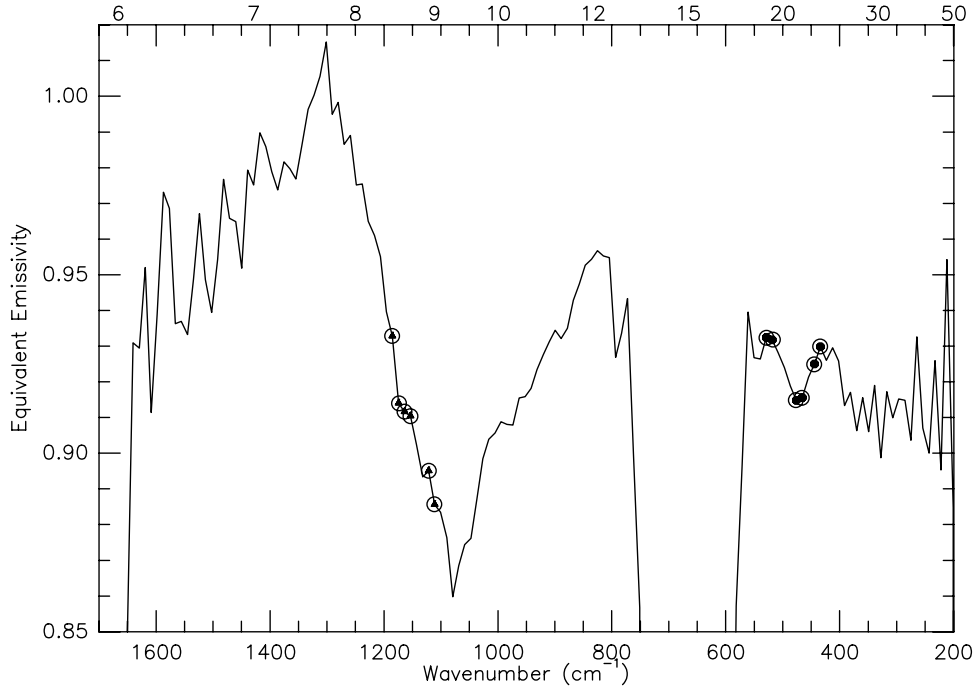

Figure 1. Average TES Spectrum from OCK 2956, incremental counter keeper (ICK) 1940, detectors 2 and 5. No atmospheric correction has been applied. The dots denote samples used for making spectral index I, and the triangles denote samples used for making spectral index II.

noise (e.g., correlations along an orbit track). The index approach is a rapid means for analyzing large quantities of data and reducing the amount of data that needs to be analyzed via a more intensive approach.

[22] Two band indices were created in an effort to find additional occurrences of the felsic material in TES data. The first index was run over TES mapping orbit data from orbit counter keeper (OCK) 1563–22,000, and the second index was run over data from OCK 1563–9500. The latter case avoids more recent TES data that are affected by a known source of noise on the MGS spacecraft which affects the spectral data in the region of that index [*Bandfield*, 2002; *Hamilton et al.*, 2003]. Data having high (>0.24) Lambert albedos representing fine particulate surfaces, emission angles >10°, surface temperatures lower than 255 K, and high-gain antenna and solar panel motions during collection were avoided.

[23] The first index (index I) is based on an emission minimum centered at ~470 cm^{-1} (Figure 1):

$$I = (\varepsilon_1 + \varepsilon_2)/2\varepsilon_3, \quad (1)$$

where ε_1 = average emissivity in TES channels 36–37 (~518 and 529 cm^{-1}), ε_2 = average emissivity in channels 28–29 (~433 and 444 cm^{-1}), and ε_3 = average emissivity in channels 31–32 (~465 and 476 cm^{-1}). These channels have the advantage of being located in a region of the spectrum that is less strongly affected by atmospheric components than channels located at higher wave numbers. This index tracks the depth of the emissivity feature at ~470 cm^{-1} relative to the emissivity values at higher and lower wave numbers than this relatively narrow absorption.

[24] The second index (index II) is based on the possible presence of quartz in the felsic lithology. Quartz is a mineral with strong spectral contrast and a distinctive doublet with a local emission maximum at ~1160 cm^{-1}. This local maximum is not observable as a strong feature in the TES emission spectrum of the felsic lithology, likely because of the strong spectral signature of the atmospheric dust in this spectral region as well as relatively low modeled quartz abundance. However, this emission maximum is such a distinctive feature in quartz that a search for this feature in TES data is potentially valuable. The emissivities used in the index are as follows using equation (1) (Figure 1): ε_1 = average emissivity in channels 92–93 (~1111 and 1122 cm^{-1}), ε_2 = average emissivity in channels 98–99 (~1174 and 1185 cm^{-1}), and ε_3 = average emissivity in channels 96–97 (~1153 and 1164 cm^{-1}). In this case, ε_3 represents the position of an emission maximum relative to the emissivities at ε_1 and ε_2. Values of the index that would be consistent with the presence of an emissivity maximum will be less than unity.

3. Results

3.1. DCS Images

[25] Over 2000 DCS images were produced according to the method described in section 2.2 and visually examined. Several images (I01221005, I01920047, I02307009, and I07887026) in the northern portion of Syrtis Major near 20°N, 65°E display unique spectral variability near the central peaks of two craters (Figures 2 and 3). No other craters in the images examined display a similar spectral signature in the region.

3.2. Surface Spectra

3.2.1. THEMIS

[26] Atmospherically corrected surface emissivity spectra were produced from THEMIS images I01221005,

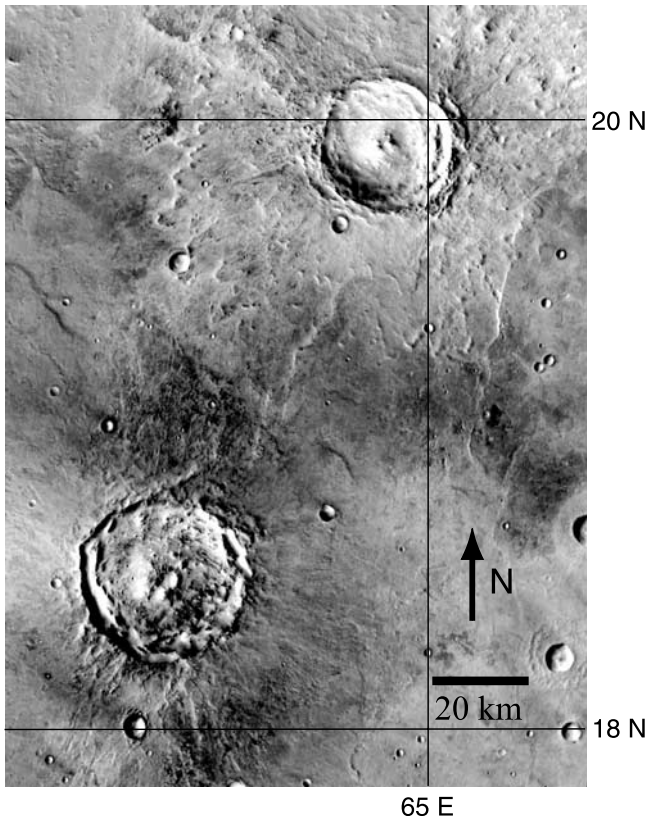

Figure 2. Mosaic of THEMIS band 9 temperature images covering the two craters with distinctive spectral signatures. The central peaks of the two craters are separated by 95 km.

I01920047, and I02307009 as detailed by *Bandfield et al.* [2004]. Surface spectra from image I07887026 were not used for this study because the surface temperature (and, as a result, signal-to-noise) is low (average surface temperature of 224 K).

[27] The plains unit located between the two craters is spectrally homogeneous and is areally large enough to use TES surface emissivity data to retrieve atmospheric properties that were applied toward recovering surface emissivity for individual THEMIS pixels as described by *Bandfield et al.* [2004]. Three distinct spectral units were identified in the THEMIS images (Figure 4) [*Bandfield et al.*, 2004]: (1) The plains surrounding the craters have a broad, relatively shallow absorption indicative of a basaltic composition. (2) Intracrater low-albedo regions have a similar spectral shape to the plains spectral unit but have a greater spectral contrast with an emissivity minimum of ~0.93 versus ~0.95. This is likely due to differences in fine particulate dust coatings present on the plains unit [*Johnson et al.*, 2002a; *Ruff and Christensen*, 2002]. (3) A spectral unit near and within the central peaks of each of the craters has deep absorptions (emissivity of 0.92–0.93) at relatively short wavelengths (THEMIS bands 4 and 5) and significantly less absorption at longer wavelengths (THEMIS bands 6–9) than the basaltic materials. The central peak spectral unit is the area of interest for this study. The central peak unit spectra from both craters in THEMIS images I01221005, I01920047, and I02307009 display similar spectral character (Figure 5).

3.2.2. TES Ratio and Surface Spectra

[28] The entire TES data set (up to OCK 23,700) was searched for spectra covering the central peaks of the two craters of interest. Under low dust and water ice opacity conditions a consistent absorption at 470 cm^{-1} could be identified visually in the uncorrected TES spectra that cover the central peak units. Spectra with this unique feature (i.e., spectral features different than the basaltic surface type 1 of *Bandfield et al.* [2000a] that is characteristic of the region) were identified and are listed in Table 2. The spectral character of the central peak unit is different from its surroundings in both the low (<550 cm^{-1}, covered by TES) and high (750–1500 cm^{-1}, covered by TES and THEMIS) wave number portions of the spectrum. The prominent atmospheric dust and water ice absorptions between ~800–1200 cm^{-1} as well as interfering spectral artifacts (~100 cm^{-1} wide Gaussian-shaped features of random sign and magnitude) present in the data past OCK ~7000 prevent the use of this spectral region for visual inspection. Unfortunately, the relatively low spatial resolution of the TES spectra (3 by ~8 km) prevents the acquisition of a "pure" central peak unit spectrum because of the small spatial extent of the central peak unit exposures (<1 by 3 km).

[29] Both 5 and 10 cm^{-1} sampling TES data were used for this analysis. The 5 cm^{-1} data were convolved to 10 cm^{-1} to allow a direct comparison of the two types of

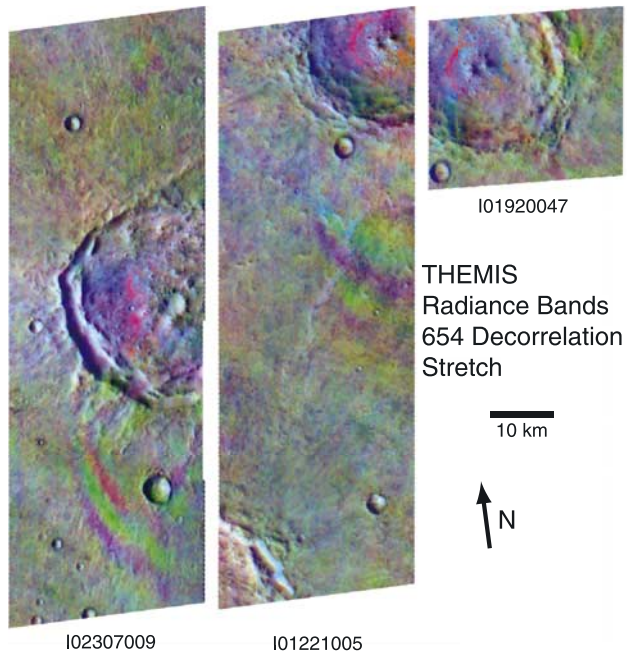

Figure 3. Decorrelation stretch images using THEMIS bands 6, 5, and 4 projected as red, green, and blue, respectively. Image I02307009 covers the southern crater displayed in Figure 2. Images I01221005 and I01920047 cover the northern crater. The central peak spectral unit appears red and orange in the images. Residual "ghosting" effects can be seen in I02307009 and I01221005 south of the craters. This amplitude of this effect is described by *Bandfield et al.* [2004]. The central peak units are free from this effect.

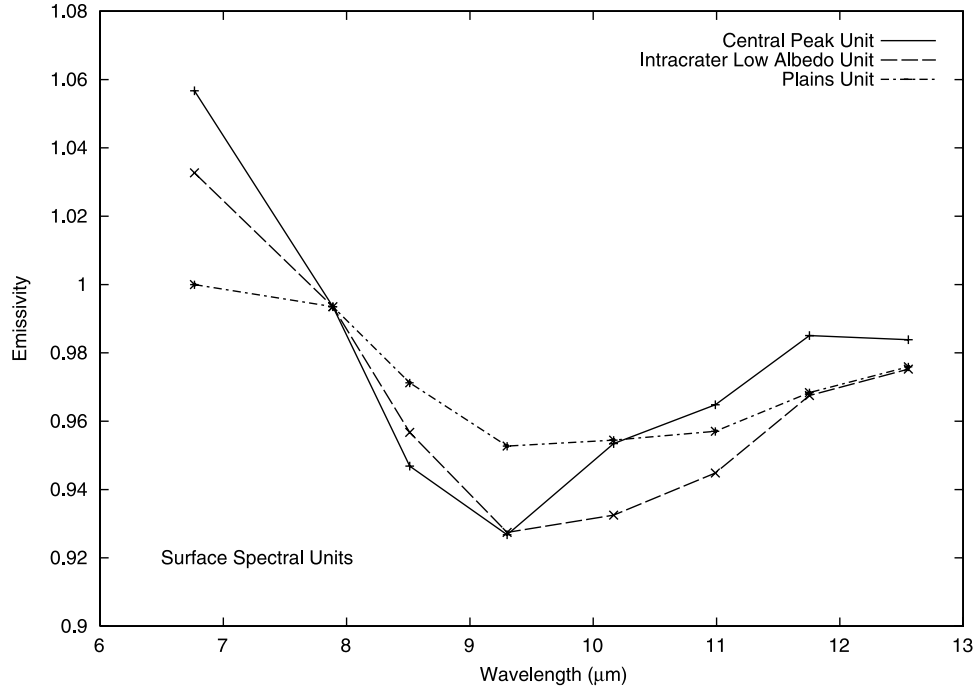

Figure 4. THEMIS image spectral units that appear in images I01221005, I01920047, and I02307009. Each spectrum is an average from all three images. Emissivity values are greater than unity for THEMIS bands 1 and 2 (6.7 μm) because band 3, which contains some atmospheric dust absorption, was used for the temperature determination.

data as well as to increase the signal-to-noise to a level comparable to the 10 cm^{-1} data. Although the 5 cm^{-1} sampling is useful for analysis of narrow spectral features such as those due to water vapor, the higher spectral resolution is not necessary for the analysis of most mineral spectral features. Examination of the 5 cm^{-1} data did not appear to provide any noticeable spectral information not identified in the 10 cm^{-1} data.

[30] The spectra of interest were ratioed against incremental counter keepers (ICKs, or, in other words, a 2 or 4 s TES observation that collects a single spectrum from each of the six detectors) immediately following or preceding

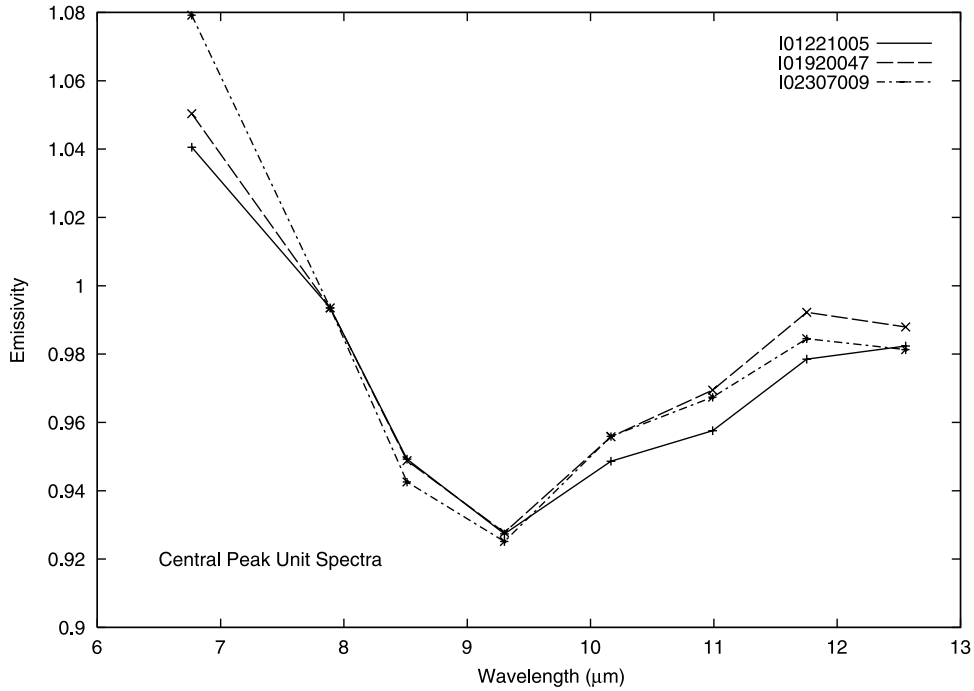

Figure 5. Central peak unit spectra from each of the three images used for this study.

Table 2. TES Spectra That Display Spectral Character Similar to the Central Peak Spectral Unit[a]

OCK	ICK	Detector	Latitude	West Longitude
2,956	1,940	2	19.9	294.3
2,956	1,940	5	19.9	294.3
11,770[b]	1,929	1/4	18.5	295.1
14,836[b]	1,939	3/6	19.9	294.5
18,456[b]	1,940	1/4	19.9	294.5
21,712	1,924	6	18.4	295.3
21,712	1,925	2	18.4	295.2
21,712	1,925	6	18.5	295.3
21,712	1,926	2	18.5	295.3
22,617	1,938	1–6	19.8	294.5
22,617	1,939	1–6	19.9	294.5

[a]Spectra were averaged on the spacecraft where multiple detectors are listed. ICK is incremental counter keeper.
[b]Shown are 5 cm^{-1} data.

each observation. In each case the central peak unit was ratioed against a spectrum covering the central plains unit. All of the spectral ratios indicate the presence of stronger spectral absorptions at 400, 470, and 800 cm^{-1} in the central peak unit. The average of the TES spectral ratios is shown in Figure 6. Though atmospheric dust and water ice as well as instrument artifacts can interfere with the spectral ratios, the average ratio spectrum also indicates that the central peak spectral unit has greater absorption present between ~1150 and 1300 cm^{-1}. Data between 860 and 1150 cm^{-1} were not included in the ratios because of instrument artifacts present past OCK 7000.

[31] Two TES spectra having low dust and water ice opacities collected before OCK 7000 cover the central peak spectral unit. Both spectra are from OCK 2956, ICK 1940 and are from TES detectors 2 and 5, which are spatially contiguous and have overlapping spatial coverage. The spectral character is similar between the two spectra, and both were averaged before analysis to increase signal-to-noise.

[32] Using the deconvolution atmospheric correction method of *Smith et al.* [2000] as applied by *Bandfield* [2002], surface spectra from the average central peak unit spectrum as well as an average of several spectra from the surrounding plains unit for comparison were retrieved (Figure 7). Mineral concentration outputs from the deconvolution atmospheric correction are listed in Table 3. Spectral fitting was limited to 350–510 cm^{-1} and 830–1300 cm^{-1}; this range is similar to previous applications [e.g., *Bandfield*, 2002] but excludes the lowest wave numbers due to numerous narrow water vapor absorptions that are present in the TES data. The atmospheric end-members used for the atmospheric correction were derived using averages of all six TES detectors. Because each TES detector has a slightly different wave number scale, there is a slight mismatch in the wave number scales between the atmospheric end-members and the average central peak unit spectrum. This mismatch can become significant in spectral regions where water vapor is present (less than ~350 cm^{-1}) and should be avoided in cases where less than all six TES detectors are used.

[33] There are significant spectral differences between the plains unit surface emissivity and the central peak unit surface emissivity. However, on the basis of both the spectral shapes and the relatively large spatial coverage of the TES spectra, there are significant contributions of the basaltic plains and intracrater low-albedo unit spectral shape to the TES central peak spectra.

[34] To isolate the central peak spectral unit signature from the TES data, some concentration of the surrounding intracrater low-albedo and plains units spectral shape must

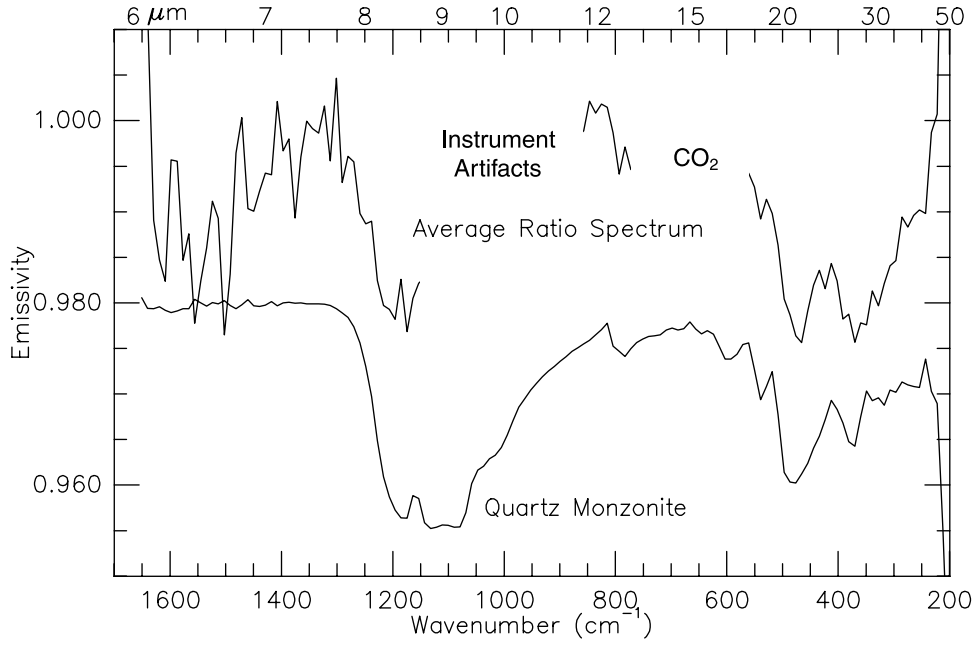

Figure 6. Average spectrum of the ratio between TES spectra that cover the central peak spectral unit (listed in Table 1) and spectra within the plains and intracrater spectral units. A laboratory emissivity spectrum of quartz monzonite (offset by 0.02 with heavily (~90%) reduced spectral contrast) is shown for comparison.

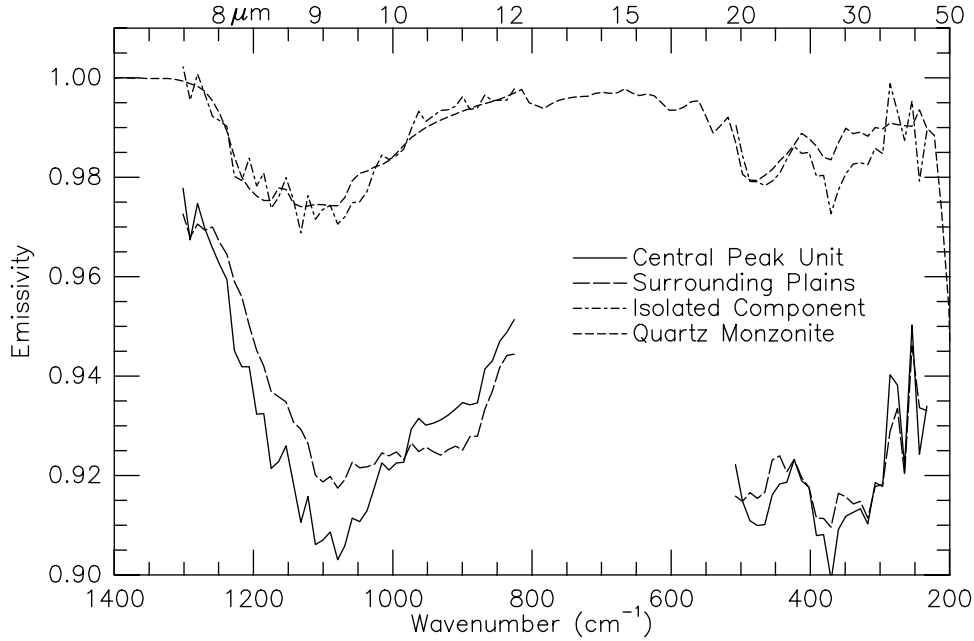

Figure 7. TES surface emissivity spectra (offset by 0.03) and isolated central peak unit spectrum. The central peak unit spectrum is the average of OCK 2956, ICK 1940, detectors 2 and 5. The plains unit spectrum is an average of OCK 2956, ICK 1936–1939, all detectors. The 300–1300 cm^{-1} spectral region was used for the deconvolution analysis.

be modeled and removed from the central peak TES spectrum. It is impossible to estimate the relative contributions of the THEMIS spectral end-members to the TES data because of the variability in spectral contrast of the plains and low-albedo intracrater unit spectral end-member as well as subpixel mixing at THEMIS spatial resolution. The spatial contribution as well as composition can be estimated, however, by assuming that the TES spectra are a linear combination of the plains and the intracrater low-albedo unit spectral signature and the spectral signature of an additional lithology.

[35] Several hundred mineral and rock spectra were tested in this manner and, in most cases, the spectral fits were poor. However, in cases involving lithologies dominated by quartz and plagioclase or quartz, plagioclase, and K-feldspar, the TES spectrum could be modeled closely (RMS error <0.0035) by a single lithology in addition to the plains and the intracrater low-albedo unit spectral signature (Table 4). For spectra with low spectral fitting errors the concentration of the plains and intracrater low-albedo unit spectral signature is nearly constant (0.83–0.93), and its contribution may be subtracted from the TES spectrum to isolate the central peak unit spectral signature (Figure 7).

3.2.3. TES Spectral Indices

[36] A global map of the value of index I does not indicate any spatially significant regions with values greater than unity that would be indicative of the prominent 470 cm^{-1} absorption. Several single to few pixel locations were identified, but in all cases, examination of the spectra indicated that these identifications were due to spurious data. On the basis of the result of this index alone, if additional sites bearing felsic lithologies are present, they are spatially limited like the detection in northern Syrtis Major.

[37] Maps of index II values in the local region surrounding the central peak spectral unit do not display the spectrally unique area prominently. Numerous pixels with low index values (signifying a possible identification) occur along orbit tracks in this area, indicating that minor noise is dominating the spectral contrast at the wavelengths of the index. Despite the inability of this index to pick out the pixels of interest in this region, the global results were examined in the event that some other site on the planet might display a strong enough spectral feature to be picked out. The global map of this index, however, does not display low index values in any spatially significant areas.

3.3. Spectral Unit Maps

[38] Spectral unit concentration maps were produced for THEMIS images I01221005, I01920047, and I02307009 (Figure 8). The maps produced for images I01221005 and I01920047 are identical to those described by *Bandfield et*

Table 3. Deconvolution Results for TES Data Covering the Central Peak Spectral Unit and the Plains Surrounding Both of the Craters[a]

	Central Peak Unit	Plains Unit
Quartz	7	–
K-feldspar/albite	9	–
Plagioclase	28	27
Pyroxene	9	31
Sheet silicate/high-Si glass	33	23
Carbonate	12	11
Sulfate	2	9

[a]The central peak unit spectra are the average of spectra from OCK 2956, ICK 1940, detectors 2 and 5. The plains unit spectrum is an average of OCK 2956, ICK 1936–1939, all detectors. Sheet silicates and high-Si glass are grouped because of their spectral similarity and the limited number of spectra used for this analysis similar to *Bandfield* [2002].

Table 4. Spectral Fitting Results Used to Isolate the Central Peak Spectral Signature From the TES Spectrum Displayed in Figure 7[a]

Sample Name	Plains and Intracrater Unit Concentration	RMS Error
Biotite granite	0.85	0.0035
Muscovite-biotite granite	0.89	0.0032
Alkalic granite	0.86	0.0033
Aplite	0.83	0.0034
Quartz monzonite	0.85	0.0033
Quartz conglomerate	0.93	0.0033
Sandstone	0.86	0.0031
Arkose	0.83	0.0029
Greywacke	0.85	0.0032
Hornfels	0.83	0.0033

[a]In all cases where RMS errors are low ($\leq$0.0035), sample mineralogies were dominated by quartz and feldspar. The contribution of the plains and low-albedo intracrater spectral unit is nearly constant where the RMS errors are low. The average concentration was used to isolate the central peak spectral signature.

al. [2004], and the concentrations and RMS error maps are similar for the southern crater image I02307009. The end-members chosen for this analysis include the TES plains unit surface emissivity, a water ice cloud spectral shape [*Bandfield et al.*, 2000b], a laboratory spectrum of quartz monzonite, and blackbody to account for variable spectral contrast between spectral units and end-members.

[39] The TES plains unit spectral shape was selected to account for the spectral signature of both the plains unit as well as the intracrater low-albedo unit because they both have a similar spectral shape. The water ice spectral shape was included to account for any spatially variable water ice cloud spectral signature present in the images. Quartz monzonite was selected as an end-member because it closely matches the central peak unit TES spectrum as described in section 3.2.2. The selection of a different quartz- and feldspar-rich lithology for the spectral unit mapping makes no significant difference in RMS errors or unit concentrations as the spectral distinctions are too fine to significantly affect the THEMIS spectra.

[40] Rock lithologies were selected as end-members rather than individual minerals for two reasons: (1) There is no indication that there are a number of independently variable mineralogies beyond the limited number of spectral units identified. (2) The limited number of spectral bands present in the THEMIS data prevents the tracking of more than a few (5–6) spectral end-members.

3.4. Crater Morphology and Thermophysical Properties

3.4.1. MOLA Elevation

[41] Both craters have a similar size and shape as indicated by MOLA data. The northern crater is 28 km in diameter, and the floor of the crater is ~1000–1100 m below the surrounding plains. The central peak of the northern crater is well defined and rises 500–600 m above the floor of the crater. The southern crater is ~30 km in diameter, and the floor of the crater is also ~1000–1100 m below the surrounding plains. The southern crater has a peak-pit structure that rises 100–300 m above the floor of the crater. There is some indication of collapse and infilling on the eastern floor of the crater.

3.4.2. VIS/IR Morphology

[42] A 36 m pixel^{-1} 5 band and an 18 m pixel^{-1} (band 3) THEMIS image that covers the northern crater central peak spectral unit were acquired (Figure 9a). The images cover the central and western portions of the crater including the central peak. In addition, there is a 3 m pixel^{-1} MOC image that corresponds to the highest concentrations of the central peak unit in the northern crater (Figure 9b). There is a slightly brighter pattern relative to its immediate surroundings present on the western edge of the central peak that corresponds to the central peak spectral unit present in the infrared image (Figure 9). However, the brightness and color of the central peak unit are not distinctive relative to other locations present in the visible/near-infrared images. The central peak unit appears smooth and featureless at 3 and 18 m pixel^{-1} sampling with no apparent outcrops, boulders, dunes, or erosional features.

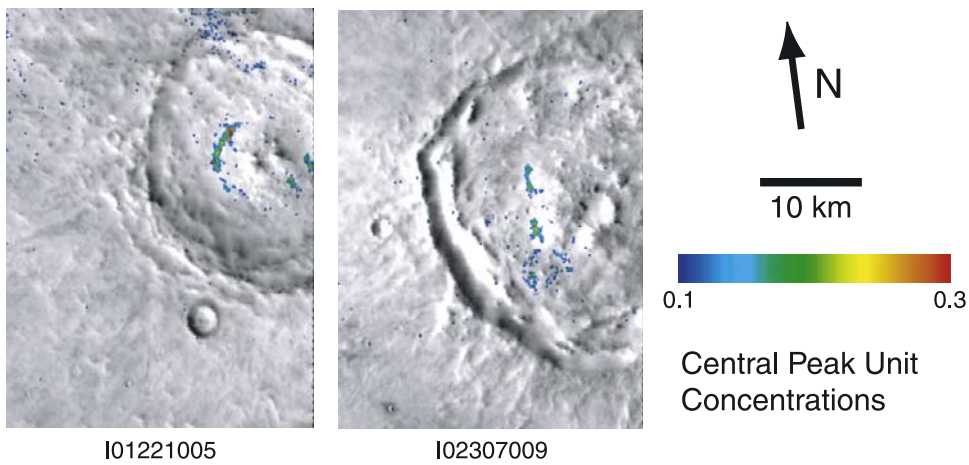

Figure 8. Central peak unit concentration maps for images I01221005 and I02307009. Colors are overlaid on temperature images for spatial context. Concentrations are similar for I01920047 and are shown by *Bandfield et al.* [2004].

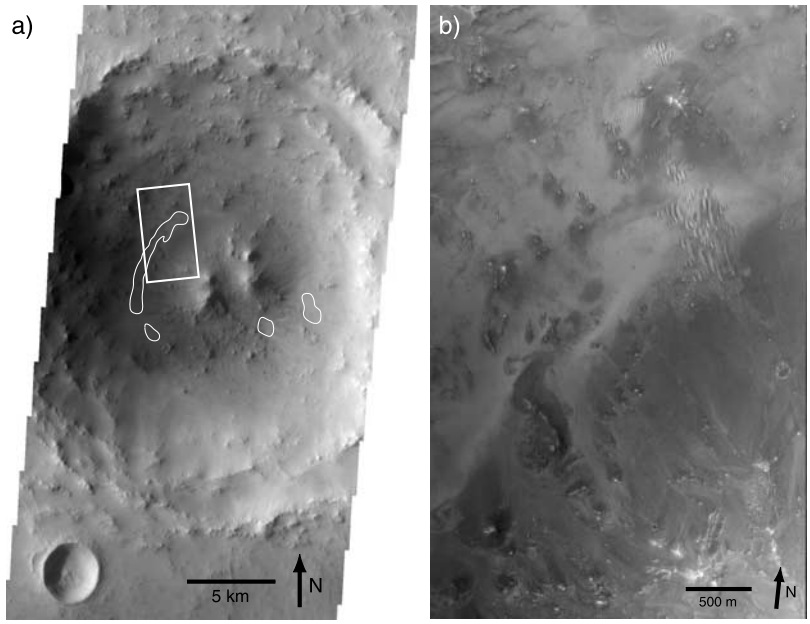

Figure 9. (a) THEMIS 18 m pixel^{-1} visible image (band 3) of the northern crater. The white box denotes the area covered in Figure 9b. The white outlines indicate the regions of elevated central peak unit concentrations shown in Figure 8. (b) MOC image R17-01195. The smooth, relatively bright region in the upper center of the image corresponds to the highest central peak unit concentrations in the northern crater. Image is courtesy of NASA/Jet Propulsion Laboratory/Malin Space Science Systems.

3.4.3. Thermal Inertia

[43] THEMIS nighttime images I01290004 and I05347011 cover the southern and northern craters, respectively. Nighttime surface temperatures (which can be used as a proxy for relative thermal inertia) for the areas that correspond to the central peak spectral unit are not distinctive relative to the surrounding terrain. The nighttime surface temperatures were input into a one point thermal inertia model (provided by H. Kieffer) along with other relevant opacity, albedo, elevation, latitude, and geometry information. Both images display surface temperatures of 185–190 K within the central peak spectral units, corresponding to thermal inertias of 240–300 and 230–290 J m^{-2} s$^{-1/2}$ K^{-1} for the southern and northern craters, respectively.

4. Discussion

4.1. Mineralogy

[44] The THEMIS and TES surface spectra from the central peak unit have similar spectral character, though the TES spectrum appears to have a significant contribution of the basaltic unit spectral shape, which is expected because of the relatively low spatial resolution of the TES data. In addition, the TES spectrum contains well-defined absorptions at <550 cm^{-1}. These absorptions are apparent in both the surface emissivity spectrum as well as the ratioed TES spectra from both craters. These spectral features can not be modeled by any combination of the two global surface spectral units [*Bandfield et al.*, 2000a], hematite [*Christensen et al.*, 2001a], Martian meteorites [*Hamilton et al.*, 2003], or olivine [*Hoefen et al.*, 2003; *Hamilton et al.*, 2003].

[45] The absorption at short wavelengths as well as the prominent absorptions at 800 and 470 cm^{-1} in the TES spectra are consistent with the presence of a quartz component on the surface. However, there are other components clearly present, and the TES spectra are a mixture of surface types. Both the deconvolution output concentrations and the isolated central peak spectral signature can be used to gain insight into the unique surface mineralogy.

[46] Output concentrations can be analyzed by noting the relative difference in the concentrations of quartz, pyroxene, sheet silicates, and feldspar compositions between the plains unit concentrations and the central peak unit concentrations (Table 3). The plains spectrum is dominated by plagioclase and pyroxene with other component concentrations similar to those previously reported within Syrtis Major [*Bandfield*, 2002]. The central peak unit displays unusually high concentrations of quartz as well as significant concentrations of sodic and calcic plagioclase, and pyroxene concentrations are low. There is also a significant elevated concentration of a sheet silicate and/or high-Si glass component. Because of the low number of TES spectra used for the analysis and the limited spatial extent of the central peak unit, it is difficult to distinguish a precise feldspar and sheet silicate/high-Si glass composition.

[47] On the basis of the deconvolution results alone it is difficult to justify concluding the presence of 7% quartz while dismissing 12% carbonate. However, as stated previously and noted by *Bandfield* [2002], there is no evidence for the prominent carbonate absorption at ~1500 cm^{-1} outside the spectral range used in the deconvolution algorithm. There is also no significant difference in the carbonate concentrations between the plains unit and the central peak unit. Where output concentration differences exist (higher

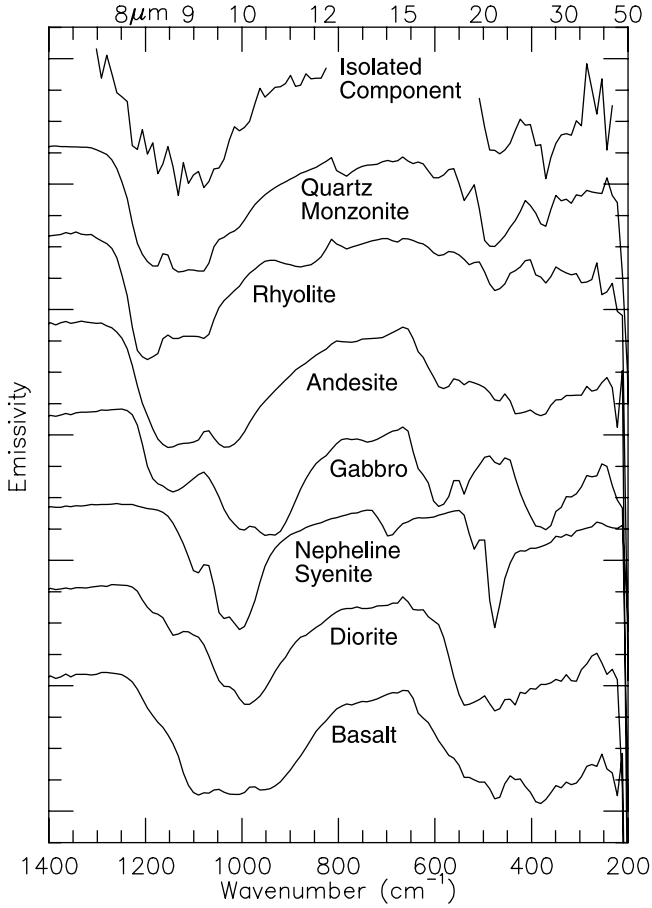

Figure 10. Isolated central peak unit spectrum from TES compared with laboratory emissivity spectra of a variety of igneous compositions. All spectra are offset and set to the same spectral contrast.

quartz, K-feldspar/albite, lower pyroxene), they are consistent with the rock types that fit both the THEMIS and the TES data.

[48] The TES central peak surface spectrum can be well fit using a linear combination of the plains unit surface spectrum and laboratory spectra of lithologies dominated by quartz and feldspar. In all cases the matching lithologies are granitoids, such as alkalai granite or quartz monzonite (Figure 10), or sedimentary rocks directly derived from granitoids, such as arkose. Several hundred mineral and rock combinations were compared, and only granitoid mineralogies were favorable matches (Figure 10).

[49] The surface spectral character, output concentrations, as well as direct spectral comparisons indicate that the central peak unit is composed of a mineralogy distinct from other previously studied Martian surfaces. The spectral signature is similar to that of granitoid compositions with quartz and feldspar, and some combination of sheet silicates and high-Si glass is present as well.

[50] A number of rock types can fit this general description. The relative imprecision of the mineralogical composition and concentrations makes it impossible to distinguish between a variety of plutonic granitoid compositions, and any composition with significant quartz and feldspar content, such as granodiorite, trondhjemite, quartz monzonite, granite, etc., is consistent with the TES and THEMIS data. Other sedimentary or metamorphic rocks derived from granitoids are also consistent with the observations, although glasses would be less likely in these other lithologies. The significant sheet silicate/high-Si glass component also could be indicative of hydrothermal alteration, weathering, and/or shock melting during crater formation. The moderate thermal inertia indicates a broken or particulate surface that is not dominated by blocks or bedrock and may be a mixture of a variety of materials.

4.2. Crater Formation

[51] Remote sensing of central peak compositions has been used to probe the composition of the lunar crust at various depths [*Pieters*, 1981; *Tompkins and Pieters*, 1999]. The central peak of a crater has been uplifted from depth and can be highly fractured, but the stratigraphy is preserved often without dominant changes in mineralogy through shock metamorphism or melting [*Melosh*, 1989]. The following relationship exists between crater diameter and the stratigraphic uplift of the central peak material [*Grieve et al.*, 1980; *Melosh*, 1989]:

$$h_{su} = 0.06D^{1.1}, \quad (2)$$

where h_{su} is the stratigraphic uplift and D is the final crater diameter in kilometers. According to this relationship the central peak material in the two craters investigated here comes from ~3–4 km depth relative to the surrounding plains.

[52] The concentration maps indicate that the central peak unit displays the highest abundances near the western perimeter of the two central peaks. It is not clear from the topography and image data if these exposures are actually part of the uplifted central peak structure. However, other exposures are clearly present on the eastern and southeastern portions of the northern crater central peak structure. Any mass wasting of the central peak structure also will tend to transport material to the base of the central peak. There is no certainty that any of the spectral units formed in place, as there are no nighttime temperatures that are indicative of a significant amount of bedrock present near either crater. An additional exposure is present to the southwest of the southern crater central peak. The presence of the low-albedo intracrater material on the western floors of the two craters may be responsible for the central peak unit exposures. The intracrater deposits are commonly composed of sand-sized particulates that can maintain dust-free surfaces through abrasion and saltation.

[53] Shock metamorphism and melting commonly occur in the cratering process. However, central peak formation requires material to maintain topographic relief that could not occur if a large portion of the surface was melted. Shock metamorphism has probably occurred in the cratering process, as it is present even in small craters such as Meteor Crater, Arizona [*Kieffer*, 1971]. It is not clear if the shocked material should be present at high concentrations over large areas. Most of the original mineralogy may be unaltered, though it is commonly highly fractured.

[54] Although high abundances of shocked materials are not necessarily in the central peak units, their spectral signatures can be similar to the minerals from which they

formed. Significant abundances of maskelynite [*Johnson et al.*, 2002b] or high-pressure silica polymorphs (coesite or stishovite) [*Michalski et al.*, 2003] may be present and not distinguishable from their source mineralogies. Using only two TES spectra with only partial spatial coverage of the central peak unit, shocked minerals such as maskelynite or coesite may be modeled with quartz and plagioclase because they have absorptions at similar wavelengths. This does not preclude the detection of shocked minerals elsewhere with the presence of greater areal coverage.

4.3. Formation of Granitoid Lithology

[55] Though the source material may have been altered by the cratering event, it is likely that the original source material was a relatively unique composition. There are hundreds of Martian craters with a similar size and morphology, including several in the immediate area. The initial examination of several thousand THEMIS images does not reveal a similar composition associated with other Martian craters or central peaks. (However, a small, isolated exposure has been recently identified with the same THEMIS spectral signature in a graben within northern Nili Fossae. This exposure is too small to be confirmed with TES data.) If the quartz-bearing material resulted from the cratering process, rather than representing a distinct crustal composition, this mineralogy should be detected more commonly.

[56] A global search using TES spectral indices also does not indicate the presence of any other exposures. However, the results of the TES indices suggest that the quartzofeldspathic lithology is difficult to identify in local exposures using simple band matching approaches. If this lithology is present elsewhere on the planet, it is likely that it is present in sufficiently low abundances and in such limited spatial extent that only techniques that examine TES spectra in their entirety will be able to identify it, and possibly only after prior detection in THEMIS data.

[57] We can speculate about the subsurface extent of this composition from the identified occurrences. Assuming that the cratering process has exposed the crust from a depth of several kilometers, and that the craters are roughly 95 km apart, it would not be unreasonable to conclude the presence of a contiguous granitoid pluton at least 95 km in size at that depth. This size is consistent with an intrusive body having a volume of hundreds of cubic kilometers.

[58] Martian meteorite and surface remote sensing observations indicate that Mars is dominated by mafic to possibly intermediate igneous compositions with no previously identified occurrences of quartzofeldspathic compositions. It is presumed that, as on Earth, basaltic magma compositions can form through partial melting of the Martian mantle [e.g., *McSween*, 2002, and references therein]. Production of significant quantities of highly differentiated, siliceous melt requires an additional mechanism such as fractional crystallization, assimilation, or partial melting of an already evolved (i.e., not ultramafic) source [e.g., *Clarke*, 1992]. Crustal assimilation plays a role in producing granitoid magmas on Earth, but the Martian crust is presumably dominated by mafic materials and is not capable of greatly enriching the silica content of a magma body. Martian meteorites (basaltic shergottites) with trace element and radiogenic isotope compositions suggesting crustal assimilation are not enriched in silica [*McSween*, 2002]. However, Martian meteorites do exhibit evidence of fractional crystallization [e.g., *Treiman et al.*, 2000]. If carried far enough, this process can produce silica-enriched magma [e.g., *Clarke*, 1992] and may be a viable mechanism for producing granitoid rocks on Mars. However, it would require enormous volumes of cumulate formation differentiating magma to produce the estimated volume of the silicic rocks from the central peak spectral unit. The production of silicic magma by fractional crystallization is enhanced if the magma is hydrous [e.g., *Grove and Kinzler*, 1986].

[59] Formation of granitoids on Earth is typically related to plate tectonics, which provides mechanisms (e.g., subduction of oceanic crust) for production of siliceous magmas. Mars displays no evidence for plate tectonics. However, the formation of Archean trondhjemites and tonalities, dominated by quartz and plagioclase, commonly occurred early in Earth's history. These granitoid rocks typically date from 2.8 to 3.8 Ga, and exposures can extend for hundreds of kilometers [*Barker*, 1979]. These silicic rocks are thought to have been produced by partial melting of thick sequences of metamorphosed basaltic source rocks (amphibolites). A steep Archean geothermal gradient resulted in the partial melting of the amphibolites at relatively low pressures, producing second-stage silica-rich magmas [e.g., *Barker*, 1979; *Clarke*, 1992]. A formation mechanism similar to that of trondhjemites and tonalities may be a viable model for the formation of the observed quartz-bearing composition on Mars. Syrtis Major may be an appropriate region that supplies the thick sequences of basaltic source rocks needed for this method of formation.

5. Conclusions

[60] THEMIS and TES data indicate a spectrally unique surface on and near the central peaks of two craters in Syrtis Major. Both deconvolution results and direct comparison with laboratory data indicate that the ratio and surface emissivity spectra are consistent with granitoid mineralogy. Specifically, emissivity spectra of igneous rocks containing high abundances of quartz and plagioclase match the Martian spectra. Deconvolution results also indicate that a sheet silicate or high-Si glass component may also be present. It is not clear how much, if any, subsequent alteration may have occurred because of weathering, coating, or hydrothermal alteration.

[61] A viable formation mechanism for this unique mineralogy on Mars may be similar to that which produces trondhjemites and tonalities on Earth. These compositions commonly formed in the Archean Era from partial melting of metamorphosed basalts without the need for plate tectonics. The two Martian exposures associated within the uplifted central peaks are 95 km apart and may indicate the extent of a subsurface granitoid pluton. Both remote sensing observations and Martian meteorites indicate that Mars has a complex igneous history with a variety of mechanisms that are likely necessary to produce the range of compositions observed to date.

[62] **Acknowledgments.** We would like to thank Laurel Cherednik, Andras Dombovari, and Kelly Bender for cheerfully enduring our data requests and collecting excellent observations. Noel Gorelick, Michael Weiss-Malik, and Benjamin Steinberg provided essential software support for the THEMIS data set. Discussions with Tim Glotch, Mike Kraft, Joe

Michalski, Michelle Minitti, Paul Niles, Deanne Rogers, and Steve Ruff helped shape the results presented here. Jeff Johnson and Mike Ramsey provided detailed formal reviews with quite a few useful suggestions.

References

Adams, J. B. (1968), Lunar and Martian surfaces: Petrologic significance of absorption bands in the near-infrared, *Science*, *159*, 1453–1455.

Adams, J. B., M. O. Smith, and P. E. Johnson (1986), Spectral mixture modeling: A new analysis of rock and soil types at the Viking Lander 1 site, *J. Geophys. Res.*, *91*, 8098–8112.

Bandfield, J. L. (2002), Global mineral distributions on Mars, *J. Geophys. Res.*, *107*(E6), 5042, doi:10.1029/2001JE001510.

Bandfield, J. L., and M. D. Smith (2003), Multiple emission angle surface-atmosphere separations of Thermal Emission Spectrometer data, *Icarus*, *161*, 47–65.

Bandfield, J. L., V. E. Hamilton, and P. R. Christensen (2000a), A global view of Martian surface compositions from MGS-TES, *Science*, *287*, 1626–1630.

Bandfield, J. L., P. R. Christensen, and M. D. Smith (2000b), Spectral data set factor analysis and end-member recovery: Application to Martian atmospheric particulates, *J. Geophys. Res.*, *105*, 9573–9588.

Bandfield, J. L., T. D. Glotch, and P. R. Christensen (2003), Spectroscopic identification of carbonate minerals in the Martian dust, *Science*, *301*, 1084–1087.

Bandfield, J. L., D. Rogers, M. D. Smith, and P. R. Christensen (2004), Atmospheric correction and surface spectral unit mapping using Thermal Emission Imaging System data, *J. Geophys. Res.*, *109*, E10008, doi:10.1029/2004JE002289.

Barker, F. (1979), Trondjhemite: Definition, environment and hypothesis of origin, in *Trondhjemites, Dacites, and Related Rocks*, edited by F. Barker, p. 1–12, Elsevier Sci., New York.

Bell, J. F., III, and R. V. Morris (1999), Identification of hematite on Mars from HST, *Lunar Planet. Sci.* [CD-ROM], *XXX*, abstract 1751.

Bell, J. F., III, et al. (2000), Mineralogic and compositional properties of Martian soil and dust: Results from Mars Pathfinder, *J. Geophys. Res.*, *105*, 1721–1755.

Christensen, P. R., et al. (1992), Thermal Emission Spectrometer experiment: Mars Observer Mission, *J. Geophys. Res.*, *97*, 7719–7734.

Christensen, P. R., et al. (2000), Detection of crystalline hematite mineralization on Mars by the Thermal Emission Spectrometer: Evidence for near-surface water, *J. Geophys. Res.*, *105*, 9632–9642.

Christensen, P. R., M. C. Malin, R. V. Morris, J. L. Bandfield, and M. D. Lane (2001a), Aqueous sedimentary mineralization of the Martian surface: Evidence for liquid water, *J. Geophys. Res.*, *106*, 23,873–23,885.

Christensen, P. R., et al. (2001b), The Mars Global Surveyor Thermal Emission Spectrometer experiment: Investigation description and surface science results, *J. Geophys. Res.*, *106*, 23,823–23,871.

Christensen, P. R., et al. (2004), The Thermal Emission Imaging System (THEMIS) for the Mars 2001 Odyssey Mission, *Space Sci. Rev.*, *110*, 85–130.

Clark, B. C., A. K. Baird, R. J. Weldon, D. M. Tsusaki, L. Schnabel, and M. P. Candelaria (1982), Chemical composition of Martian fines, *J. Geophys. Res.*, *87*, 10,059–10,067.

Clarke, D. B. (1992), *Granitoid Rocks*, 283 pp., Chapman and Hall, New York.

Foley, C. N., T. Economou, and R. N. Clayton (2003), Final chemical results from the Mars Pathfinder alpha proton X-ray spectrometer, *J. Geophys. Res.*, *108*(E12), 8096, doi:10.1029/2002JE002019.

Geissler, P. E., R. B. Singer, G. Komatsu, S. Murchie, and J. Mustard (1993), An unusual spectral unit in West Candor Chasma: Evidence for aqueous or hydrothermal alteration in the Martian canyons, *Icarus*, *106*, 380–391.

Gillespie, A. R. (1992), Spectral mixture analysis of multispectral thermal infrared images, *Remote Sens. Environ.*, *42*, 137–145.

Gillespie, A. R., A. B. Kahle, and R. E. Walker (1986), Color enhancement of highly correlated images: I. Decorrelation and HIS contrast stretches, *Remote Sens. Environ.*, *20*, 209–235.

Grieve, R. A. F., P. B. Robertson, and M. R. Dence (1980), Constraints on the formation of ring impact structures, based on terrestrial data, *Geochim. Cosmochim. Acta Suppl.*, *15*, 37–58.

Grove, T. L., and R. J. Kinzler (1986), Petrogenesis of andesites, *Annu. Rev. Earth Planet. Sci.*, *14*, 417–454.

Hamilton, V. E., M. B. Wyatt, H. Y. McSween Jr., and P. R. Christensen (2001), Analysis of terrestrial and volcanic compositions using thermal emission spectroscopy: II. Application to Martian surface spectra from the Mars Global Surveyor Thermal Emission Spectrometer, *J. Geophys. Res.*, *106*, 14,733–14,746.

Hamilton, V. E., P. R. Christensen, H. Y. McSween Jr., and J. L. Bandfield (2003), Searching for the source regions of Martian meteorites using MGS TES: Integrating Martian meteorites into the global distribution of igneous materials on Mars, *Meteorit. Planet. Sci.*, *38*, 871–885.

Hoefen, T. M., R. N. Clark, J. L. Bandfield, M. D. Smith, J. C. Pearl, and P. R. Christensen (2003), Discovery of olivine in the Nili Fossae region of Mars, *Science*, *302*, 627–630.

Johnson, J. R., P. R. Christensen, and P. G. Lucey (2002a), Dust coatings on basaltic rocks and implications for thermal infrared spectroscopy of Mars, *J. Geophys. Res.*, *107*(E6), 5035, doi:10.1029/2000JE001405.

Johnson, J. R., F. Hörz, P. G. Lucey, and P. R. Christensen (2002b), Thermal infrared spectroscopy of experimentally shocked anorthosite and pyroxenite: Implications for remote sensing of Mars, *J. Geophys. Res.*, *107*(E10), 5073, doi:10.1029/2001JE001517.

Kieffer, S. W. (1971), Shock metamorphism of the Coconino Sandstone at Meteor Crater, Arizona, *J. Geophys. Res.*, *76*, 5449–5473.

Kraft, M. D., J. R. Michalski, and T. G. Sharp (2004), High-silica rock coatings: TES surface-type 2 and chemical weathering on Mars, *Lunar Planet. Sci.* [CD-ROM], *XXXV*, abstract 1936.

Malin, M. C., and K. S. Edgett (2001), Mars Global Surveyor Mars Orbiter Camera: Interplanetary cruise through primary mission, *J. Geophys. Res.*, *106*, 23,429–23,570.

McCord, T. B., R. N. Clark, and R. B. Singer (1982), Mars: Near-infrared spectral reflectance of surface regions and compositional implications, *J. Geophys. Res.*, *87*, 3021–3032.

McSween, H. Y., Jr. (1994), What have we learned about Mars from SNC meteorites, *Meteoritics*, *29*, 757–779.

McSween, H. Y., Jr. (2002), The rocks of Mars, from far and near, *Meteorit. Planet. Sci.*, *37*, 7–26.

McSween, H. Y., Jr., and K. Keil (2000), Mixing relationships in the Martian regolith and the composition of globally homogeneous dust, *Geochim. Cosmochim. Acta*, *64*, 2155–2166.

McSween, H. Y., et al. (1999), Chemical, multispectral, and textural constraints on the composition and origin of rocks at the Mars Pathfinder landing site, *J. Geophys. Res.*, *104*, 8679–8716.

Melosh, H. J. (1989), *Impact Cratering: A Geologic Process*, 245 pp., Oxford Univ. Press, New York.

Merenyi, E., R. B. Singer, and J. S. Miller (1996), Mapping of spectral variations on the surface of Mars from high resolution telescopic images, *Icarus*, *124*, 280–295.

Michalski, J. R., M. D. Kraft, T. Diedrich, T. G. Sharp, and P. R. Christensen (2003), Thermal emission spectroscopy of the silica polymorphs and considerations for remote sensing of Mars, *Geophys. Res. Lett.*, *30*(19), 2008, doi:10.1029/2003GL018354.

Minitti, M. E., J. F. Mustard, and M. J. Rutherford (2002), Effects of glass content and oxidation on the spectra of SNC-like basalts: Applications to Mars remote sensing, *J. Geophys. Res.*, *107*(E5), 5030, doi:10.1029/2001JE001518.

Morris, R. V., et al. (2000), Mineralogy, composition, and alteration of Mars Pathfinder rocks and soils: Evidence from multispectral, elemental, and magnetic data of terrestrial analogue, SNC meteorite, and Pathfinder samples, *J. Geophys. Res.*, *105*, 1757–1817.

Morris, R. V., et al. (2004), A first look at the mineralogy and geochemistry of the MER-B landing site in Meridiani Planum, *Lunar Planet. Sci.* [CD-ROM], *XXXV*, abstract 2179.

Murchie, S., J. Mustard, J. Bishop, J. Head, C. Pieters, and S. Erard (1993), Spatial variations in the spectral properties of bright regions on Mars, *Icarus*, *105*, 454–468.

Mustard, J. F., and C. M. Pieters (1987), Abundance and distribution of ultramafic microbreccia in Moses Rock Dike: Quantitative application of mapping spectroscopy, *J. Geophys. Res.*, *92*, 10,376–10,390.

Mustard, J. F., S. Erard, J. P. Bibring, J. W. Head, S. Hurtrez, Y. Langevin, C. M. Pieters, and C. J. Sotin (1993), The surface of Syrtis Major: Composition of the volcanic substrate and mixing with altered dust and soil, *J. Geophys. Res.*, *98*, 3387–3400.

Mustard, J. F., S. Murchie, S. Erard, and J. Sunshine (1997), In situ compositions of Martian volcanics: Implications for the mantle, *J. Geophys. Res.*, *102*, 25,605–25,616.

Pieters, C. M. (1981), Copernicus crater central peak: Lunar mountain of unique composition, *Science*, *215*, 59–61.

Ramsey, M. S. (2002), Ejecta distribution patterns at Meteor Crater, Arizona: On the applicability of lithologic end-member deconvolution for spaceborne thermal infrared data of Earth and Mars, *J. Geophys. Res.*, *107*(E8), 5059, doi:10.1029/2001JE001827.

Ramsey, M. S., P. R. Christensen, N. Lancaster, and D. A. Howard (1999), Identification of sand sources and transport pathways at Kelso Dunes, California using thermal infrared remote sensing, *Geol. Soc. Am. Bull.*, *111*, 636–662.

Ruff, S. W. (2004), Spectral evidence for zeolite in the dust on Mars, *Icarus*, *168*, 131–143.

Ruff, S. W., and P. R. Christensen (2002), Bright and dark regions on Mars: Particle size and mineralogical characteristics based on Thermal Emission

Spectrometer data, *J. Geophys. Res.*, *107*(E12), 5127, doi:10.1029/2001JE001580.

Singer, R. B., and H. Y. McSween Jr. (1993), The igneous crust of Mars: Compositional evidence from remote sensing and the SNC meteorites, in *Resources of Near-Earth Space*, edited by J. Lewis, M. S. Matthews, and M. L. Guerrieri, pp. 709–736, Univ. of Ariz. Press, Tucson.

Singer, R. B., T. B. McCord, R. N. Clark, J. B. Adams, and R. L. Huguenin (1979), Mars surface composition from reflection spectroscopy: A summary, *J. Geophys. Res.*, *84*, 8415–8425.

Smith, D. E., et al. (2001), Mars Orbiter Laser Altimeter (MOLA): Experiment summary after the first year of global mapping of Mars, *J. Geophys. Res.*, *106*, 23,689–23,722.

Smith, M. D., J. L. Bandfield, and P. R. Christensen (2000), Separation of atmospheric and surface spectral features in Mars Global Surveyor Thermal Emission Spectrometer (TES) spectra, *J. Geophys. Res.*, *105*, 9589–9607.

Soderblom, L. A., K. Edwards, E. M. Eliason, E. M. Sanchez, and M. P. Charette (1978), Global color variations on the Martian surface, *Icarus*, *34*, 446–464.

Tompkins, S., and C. M. Pieters (1999), Mineralogy of the lunar crust: Results from Clementine, *Meteorit. Planet. Sci.*, *34*, 25–41.

Toulmin, P., A. K. Baird, B. C. Clark, K. Keil, H. J. Rose, R. P. Christian, P. H. Evans, and W. C. Kelliher (1977), Geochemical and mineralogical interpretation of the Viking inorganic chemical results, *J. Geophys. Res.*, *82*, 4625–4634.

Treiman, A. H., J. D. Gleason, and D. D. Bogard (2000), The SNC meteorites are from Mars, *Planet. Space Sci.*, *48*, 1213–1230.

Wyatt, M. B., and H. Y. McSween Jr. (2002), Spectral evidence for weathered basalt as an alternative to andesite in the northern lowlands of Mars, *Nature*, *417*, 263–266.

J. L. Bandfield, Mars Space Flight Facility, Arizona State University, Tempe, AZ 85287-6305, USA. (joshband@asu.edu)

P. R. Christensen, Department of Geological Sciences, Arizona State University, Campus Box 871404, Tempe, AZ 85287-1404, USA.

V. E. Hamilton, Hawai'i Institute of Geophysics and Planetology, University of Hawai'i, 2525 Correa Road, Post 524B, Honolulu, HI 96822, USA.

H. Y. McSween Jr., Department of Earth and Planetary Sciences, University of Tennessee, Knoxville, TN 37996-1410, USA.